https://doi.org/10.5194/essd-2026-617
Preprint. Discussion started: 25 November 2026
© Author(s) 2026. CC BY 4.0 License.



Open Access Earth System Science Data Discussions

The Improvement of the Reconstruction of OHC Based on DINCAE

Tao Xie[1,2], Wenying Mao[3], Hengqian Yan[*4,5] , Mei Hong[4], Jian Li[3],Wenmei Li[1], Yixiang Chen[1], Yi Huang[1], Xiaobo Zhu[1],Haili Li[1]

[1] School of Internet of Things, Nanjing University of Posts and Telecommunications, 210003, Nanjing, Jiangsu, China

[2] Laboratory for Regional Oceanography and Numerical Modeling, Qingdao Marine Science and Technology Center, 266200, Qingdao, Shandong Province, China

[3] School of Remote Sensing and Geomatics Engineering, Nanjing University of Information Science and Technology, Nanjing , Jiangsu 210044, China;

[4] College of Meteorology and Oceanography, National University of Defense Technology, Changsha, Hunan 410073, China

[5]Key Laboratory of Marine Environmental Information Technology, MEIT, Tianjin 300171, China

Correspondence: Yan Hengqian(yanhengqian18@nudt.edu.cn)

Abstract. Owing to its immense volume and high specific heat capacity, the ocean absorbs most of the excess heat associated with Earth's energy imbalance and is therefore the principal reservoir of heat in the climate system (Zhu et al., 2024). Ocean heat content (OHC) is therefore a key metric for quantifying heat storage and redistribution. Conventional gridding methods can introduce substantial uncertainty when sparse in situ observations are mapped with prescribed covariance structures. Here, the Data-Interpolating Convolutional Auto-Encoder (DINCAE) is applied to quality-controlled CODC-v2 profiles to reconstruct monthly three-dimensional ocean temperature fields and derive the OHC-DREC dataset for 60°S–60°N from January 1960 to October 2024. Validation against a withheld 15% subset of observations gives an MAE of 0.58 °C, RMSE of 0.87 °C, correlation of 0.994, and R^2 of 0.989. The reconstructed OHC reproduces the climatological annual cycle, long-term warming, and major spatial patterns represented by established OHC products. Its interannual heat-uptake variability is also consistent with the independent Clouds and the Earth's Radiant Energy System (CERES) Earth energy imbalance record. Sea surface temperature and El Niño–Southern Oscillation diagnostics indicate that the reconstruction retains physically coherent variability during the data-sparse pre-Argo period. OHC-DREC is available from Zenodo at https://doi.org/10.5281/zenodo.21758104 (Xie et al., 2026).

https://doi.org/10.5194/essd-2026-617
Preprint. Discussion started: 25 November 2026
© Author(s) 2026. CC BY 4.0 License.



Open Access Earth System Science Data Discussions

1. Introduction

Ocean heat content (OHC) is the principal indicator used to quantify the accumulation of excess energy in the climate system. Because the ocean absorbs the dominant share of the Earth energy imbalance, OHC integrates subsurface thermal changes that cannot be inferred from sea-surface temperature alone (Rhein et al., 2013; von Schuckmann et al., 2016; Cheng et al., 2019). Sea surface temperature and ENSO are retained only as process-based diagnostics of the reconstructed three-dimensional field, not as the central research objective.

Since the Industrial Revolution, anthropogenic greenhouse-gas emissions have increased atmospheric greenhouse-gas concentrations and disrupted Earth's radiative balance (Dergiades et al., 2016; Liu, 2003). OHC is therefore one of the most important indicators of global warming (von Schuckmann et al., 2016; Cheng et al., 2019).. Compared with sea-surface temperature (SST), OHC integrates thermal changes throughout the water column and more directly reflects energy accumulation in the Earth system (Palmer et al., 2011). During the early-2000s slowdown in the rise of global-mean surface temperature, continued OHC increase showed that energy continued to accumulate in the ocean and was redistributed toward deeper layers (Meehl et al., 2011; Liu et al., 2016; Loeb et al., 2018).

In addition, the evolution of ENSO events is closely related to the distribution of ocean heat content. Its prediction accuracy even exceeds that of SST, making it one of the main methods for tropical climate prediction (Jin, 1997). Therefore, OHC is not only a key indicator of the Earth system's energy imbalance, but also the physical basis for analyzing air-sea interactions, which can regulate the variability of global and regional climate modes and estimate the response to extreme climate events (Forney et al., 2025; Colfescu et al., 2024).

Reliable OHC estimation remains challenging because ocean observations are highly uneven in space and time (Cheng et al., 2017). Before the near-global deployment of Argo after 2005, temperature observations relied mainly on ship-based measurements, expendable bathythermographs (XBTs), mechanical bathythermographs (MBTs), and conductivity--temperature--depth instruments (Abraham et al., 2013). Sampling was concentrated along Northern Hemisphere shipping routes, whereas the Southern Hemisphere, the Southern Ocean, and the deep ocean remained sparsely observed. Instrumental biases introduce an additional source of uncertainty. In particular, errors in XBT fall-rate equations and temperature sensors can produce systematic temperature and depth biases (Gouretski and Reseghetti, 2010). Differences in instrument type, calibration, depth coverage, quality control, and historical bias correction consequently contribute to discrepancies among OHC products (Ishii and Kimoto, 2009; Levitus et al., 2012; Wang et al., 2018).

https://doi.org/10.5194/essd-2026-617
Preprint. Discussion started: 25 November 2026
© Author(s) 2026. CC BY 4.0 License.



In addition to observational errors, OHC estimates are sensitive to every stage of the mapping procedure used to convert irregular profiles into gridded fields. Objective interpolation, data assimilation, and statistical mapping differ in their background covariance, first guess, vertical interpolation, quality control, and historical bias-correction assumptions (Boyer et al., 2016; Li et al., 2022). These design choices can produce materially different OHC trends, particularly before Argo when observations were sparse and geographically concentrated. A climatological first guess may draw poorly sampled regions toward the mean state, suppressing interannual variability and long-term change; model-informed covariance can reduce sampling noise but inherits the structural biases of the model background (Cheng & Zhu, 2016a; Cheng & Zhu, 2016b). The consequences are most acute in the Southern Ocean, marginal seas, high-latitude and ice-covered waters, energetic boundary currents, and the deep ocean, where profile coverage remains limited.where profile coverage remains limited(Allison et al., 2019)

Machine-learning approaches provide a complementary route because they can learn nonlinear spatial and temporal relationships that are difficult to specify in a prescribed covariance model. Su et al. (2021) used remote-sensing variables and Argo data to reconstruct a long OHC record, while Lu and Su (2023) described neural-network retrieval of OHC at several depth ranges. Lyman and Johnson (2023) produced high-resolution OHC anomaly maps using random-forest regression and satellite predictors. These studies demonstrate the value of data-driven methods, but many rely on satellite predictors and Argo-era training data, which limits their direct use for the earlier historical period and can transfer predictor-specific biases into the OHC estimate.

The present study addresses this gap by applying DINCAE directly to the quality-controlled, bias-corrected CODC-v2 profile-temperature archive. The method reconstructs a temporally continuous three-dimensional temperature field from 1960 onward without using satellite altimetry, sea-surface height, or CERES energy-budget data as predictors. The derived OHC is evaluated against withheld profile observations, independent gridded OHC products, ENSO-related variability, and the CERES Earth energy imbalance. This combination isolates the contribution of profile-based nonlinear reconstruction while retaining independent physical checks.

2.Dataset

2.1 Input profile data

https://doi.org/10.5194/essd-2026-617
Preprint. Discussion started: 25 November 2026
© Author(s) 2026. CC BY 4.0 License.



Open Access Earth System Science Data Discussions

This study uses CODC-v2 (CAS Oceanographic Data Center, Global Ocean Science Database, version 2) profile temperature observations supplied by the Institute of Atmospheric Physics, Chinese Academy of Sciences, as reconstruction input (Tan et al., 2023; Zhang et al., 2024; Tan et al., 2025). CODC-v2 is a profile-level archive assembled from the World Ocean Database and supplemented with Global Temperature and Salinity Profile Program updates. It contains observations from 14 instrument classes, including XBT, CTD, Argo, gliders, and buoys, and covers records from 1940 onward.

Reliability of the input archive is essential because DINCAE learns the spatial and temporal structure from retained observations and any residual profile bias can propagate into reconstructed temperature and depth-integrated OHC. CODC-v2 applies its CODC-QC procedure, including gross-error, spike, gradient, and local-climatology checks, to identify implausible observations while retaining valid profiles. Instrument-dependent bias corrections are applied to historical measurements, including bathythermograph observations, before the gridding step. These procedures reduce known temporal inhomogeneities that otherwise affect historical OHC estimates.

For this study, profiles from January 1960 to October 2024 and depths from 0 to 2000 m are binned to a 1° × 1° monthly grid with 79 vertical layers. Monthly binning averages valid profile temperatures within each spatial cell and preserves a land-ocean mask. The resulting fields contain longitude, latitude, time, depth, temperature, and masks, which provide the inputs required for reconstruction and profile-level validation(Merchel et al., 2025)..

2.2 Data products used for intercomparison

This study involves multiple sets of global ocean reanalysis and observational datasets. In terms of SST,NOAA's ERSSTv5 is used (Palmer et al. 2007; Domingues et al. 2008). It corrects historical ship observations based on modern drifting buoys and combines the EOT method with reduced spatial filtering to improve the reconstruction ability of sea temperature anomalies in polar and tropical regions; JMA's COBE2 is reconstructed based on OI and EOF and integrates sea-ice information; the UK Met Office's HadISST fuses in-situ and satellite data and uses the RSOI method to reconstruct long-term modes (Ishii et al. 2005). In terms of OHC, IAPv4.2 is used, which is based on the improved ensemble optimal interpolation and the CMIP5 multi-model background error covariance (Cheng et al. 2017; Cheng et al. 2016; Cheng et al. 2024); NOAA NCEI provides the stratified heat content for 0–700m and 0–2000m (Levitus et al. 2012); EN4.2 undergoes strict quality control and uses the objective analysis method to construct a high-quality data field (Good et al. 2013); Ishii corrects the systematic bias of XBT, converts observational data into grid data through objective analysis techniques, and then uses statistical methods to reconstruct and fill in data-sparse regions (Ishii et al. 2009); BOA-Argo uses the improved Barnes step-by-step correction method (Li et al. 2017); GDCSM-ARGO uses an anisotropic background error correlation scheme (Zhang et al. 2022); RG_Argo is generated through optimal interpolation (Roemmich et al. 2009). Other auxiliary data include the ONI index calculated based on ERSSTv5 (3-month moving average of SST anomalies in the central and eastern equatorial Pacific, used for ENSO monitoring) and the NASA CERES EBAF radiation dataset (Kato et al. 2018) .

https://doi.org/10.5194/essd-2026-617
Preprint. Discussion started: 25 November 2026
© Author(s) 2026. CC BY 4.0 License.



The SST and OHC products play different roles in this study and are listed separately below. SST products are used only to assess SST and ENSO diagnostics, whereas OHC products are used for the principal comparison of annual cycles, long-term trends, spatial patterns, and energy-budget consistency. All datasets are harmonized to the stated study period and, where needed, resampled to the 1° × 1° analysis grid.

Tables 1 and 2 provide the data inventory. Table 1 contains the SST diagnostic products. Table 2 contains the OHC comparison products with depth coverage listed as a separate column, as required for interpreting vertically integrated heat-content differences.

Table 1. SST products used for SST and ENSO diagnostics

Dataset	Source	Period used	Resolution	Mapping or processing
ERSSTv5	NOAA	1854 onward	2° × 2°, monthly	EOT reconstruction and reduced-space filtering
COBE2	JMA	1850 onward	1° × 1°, monthly	Optimal interpolation, EOF, and sea-ice information
HadISST	UK Met Office	1870 onward	1° × 1°, monthly	In situ/satellite fusion and RSOI

Table 2. OHC products used for reconstruction evaluation and physical-consistency analysis

Dataset	Source	Period used	Resolution	Depth coverage	Mapping or processing
IAPv4.2	IAP	1940 onward	1° × 1°, monthly	0–6000 m 79 layers; 0–6000 m	Improved ensemble optimal interpolation with CMIP background covariance
NCEI	NOAA/NCEI	1955 onward	1°× 1°; monthly/annual	0–2000 m; 0–2000 m	Product-provided gridded OHC and bias correction
EN4.2	UK Met Office	1900 onward	1° × 1°, monthly	0–5500 m; 42 layers 0–5500 dbar	Quality-controlled profiles and objective analysis
Ishii	JMA	1955 onward	1° × 1°, monthly/annual	0-3000 m;28 layers; 0–3000 m	XBT correction, objective analysis, and statistical infilling
BOA-Argo	Argo product	2004 onward	1° × 1°, monthly	0-1975 m;58 layers; 0–1975 dbar	Barnes successive corrections
GDCSM-Argo	Argo product	2004 onward	1° × 1°	0-2000 m;58 layers; 0–2000 m	Gradient-dependent optimal interpolation
RG-Argo	Argo product	2004 onward	1° × 1°, monthly	0-1975 m;58 layers; 0–1975 dbar	Optimal interpolation

All comparison datasets are standardized before analysis. Monthly records are restricted to the period required for each comparison, with the principal long-term analyses covering from January 1960 to October 2024. Products with different native grids are resampled to the common 1° × 1° analysis grid using nearest-neighbour interpolation. The study domain is restricted to 60° S--60° N and 180° W--180° E, consistent with the reconstruction domain. This harmonization provides common temporal and spatial coordinates while avoiding additional smoothing of the original gridded fields..

3 Data processing and methods

3.1 Spatiotemporal distribution of profile observations

The spatiotemporal sampling of the profile observations used for reconstruction is highly

https://doi.org/10.5194/essd-2026-617
Preprint. Discussion started: 25 November 2026
© Author(s) 2026. CC BY 4.0 License.



inhomogeneous. Sampling decreases systematically with depth: missing rates are 92.63% at 1 m and 88.73% at 5 m, rise to 91.33% at approximately 500 m and 94.04% at 1000 m, and reach 99.48% at 2000 m. Thus, sampling generally becomes sparser below the near-surface layers. The temporal pattern reflects the evolution of the observing system, with observations concentrated along shipping routes before widespread Argo deployment and substantially improved spatial coverage after the early 2000s.. These sampling limitations are important for interpreting reconstruction uncertainty, particularly at depth and during the pre-Argo period (Cheng et al., 2024).

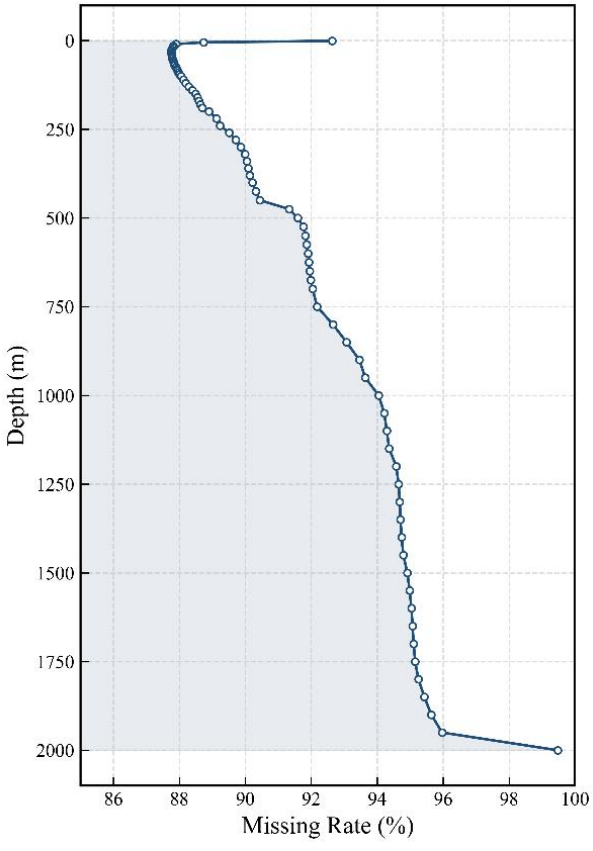

Figure 1: Mean fraction of missing monthly temperature values as a function of depth for the 60° S--60° N reconstruction domain during January 1960--October 2024.

3.2 Reconstruction method

3.2.1 DINCAE framework and observational sampling

DINCAE is a data-interpolating convolutional auto-encoder designed to train directly on

https://doi.org/10.5194/essd-2026-617
Preprint. Discussion started: 25 November 2026
© Author(s) 2026. CC BY 4.0 License.



incomplete geophysical fields while estimating reconstruction uncertainty (Barth et al., 2020). DINCAE 2.0 extends this approach by introducing additive skip connections and refinement steps that preserve fine-scale structure during decoding (Barth et al., 2022). The temporal variation in the available sampling used by the reconstruction is shown in Fig. 2.

"DINCAE 2.0 is used here to reconstruct monthly gridded ocean temperature at each of the 79 target depths. Its convolutional encoder--decoder follows a U-Net-like structure. The encoder successively reduces spatial resolution while extracting features from the masked input fields, whereas the decoder restores the original resolution. Additive skip connections transfer fine-scale spatial information from the encoder to the decoder.

3.2.2 Binned-data preparation

The January 1960--October 2024 profile archive is first restricted to 60°S-60°N and 0-2000 m. Valid observations are assigned to 1°cells and monthly bins at the 79 target depths. For each depth, the binned field has 120 latitude cells by 360 longitude cells and 778 monthly samples. Temperature, latitude, longitude, time, and the land-ocean mask are stored together. Missing ocean values remain missing rather than being set to zero; land points are excluded from training and evaluation. This separation prevents the model from interpreting missingness as temperature information.

3.2.3 Model training

DINCAE 2.0 uses a convolutional encoder-decoder with additive skipconnections and refinement steps (Barth et al., 2022). Five internalencoder levels used 3 × 3 convolutional kernels with 32, 64, 128, 256,and 512 filters, respectively, and 2 × 2 mean-pooling. The decoderrestored spatial resolution using nearest-neighbour upsampling andconvolution, with the default additive skip connections transferringfeatures from the encoder. Hidden convolutional layers used theRectified Linear Unit activation and the output layer was linear. Theinput time window contained three consecutive monthly fields. Theprescribed observational-error standard deviation was 1, and Gaussianjitter with a standard deviation of 0.05 was added during training.

DINCAE predicts the temperature anomaly scaled by inverse error variancetogether with the logarithm of inverse error variance. Trainingminimizes the Gaussian negative log-likelihood at valid target locationsrather than a conventional L1 or L2 loss. The production configurationused two-dimensional convolution, nearest-neighbour upsampling, and atwo-step refinement model with loss weights of 0.3 and 0.7. The Adamoptimizer retained its DINCAE default initial learning rate of 0.001with no decay. Training used 1000 epochs, a batch size of 32, andgradient clipping at 5.0. No L1 or L2 weight regularisation was applied;instead, Gaussian jitter ($\sigma = 0.05$) was added to the input fields duringtraining as a stochastic regulariser. The reconstruction fields from thefinal epoch are used for all subsequent analyses.

DINCAE 2.0 uses a convolutional encoder-decoder with additive skip connections and refinement

https://doi.org/10.5194/essd-2026-617
Preprint. Discussion started: 25 November 2026
© Author(s) 2026. CC BY 4.0 License.



steps (Barth et al., 2022). Five internal encoder levels used 3 × 3 convolutional kernels with 32, 64, 128.

3.2.4 Prediction and OHC calculation

The selected model is applied to every monthly binned temperature field at all depths to generate complete three-dimensional fields. OHC is calculated by trapezoidal integration over depth using a constant seawater density of 1027 kg m^{-3} and specific heat capacity of 3991.9 J kg^{-1} K^{-1}.The value at 1 m is extrapolated to the sea surface, grid-cell heat content is multiplied by spherical grid-cell area, and the grid-cell values are summed over the analysis domain; results are reported in zettajoules (1 ZJ = 10^{21} J).

4 Results

4.1 Assessment against withheld observations

For the 10 m example, the reconstruction input contains 778 monthly fields of 120 × 360 grid cells and has a mean missing fraction of approximately 84%. Monthly missingness ranges from about 76.6% to more than 96.5%.

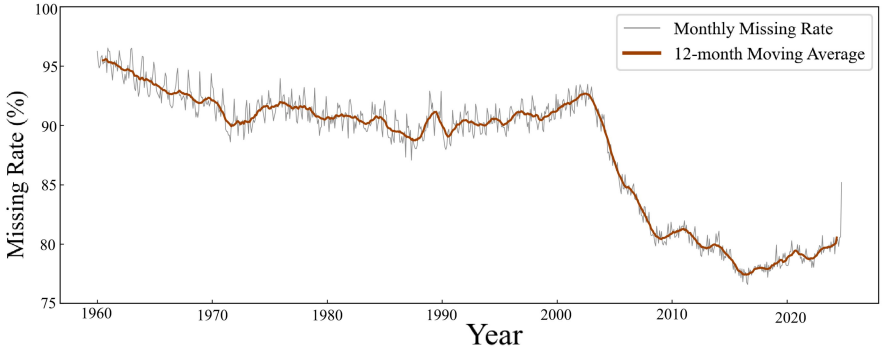

Figure 2: Monthly fraction of missing 10 m temperature observations from January 1960 to October 2024.

To illustrate how observational coverage and reconstruction quality have evolved with the changing observing system, Figure 3 compares the available 10 m temperature observations (left column) with the corresponding DINCAE reconstructions (right column) for four selected months: January 1960, 1980, 2000, and 2020. Sampling in January 1960 is sparse and concentrated along shipping routes and continental margins. Coverage expands by 1980 and 2000 and becomes substantially more uniform by 2020 following the widespread deployment of Argo (Xie 1994). Nevertheless, data gaps remain, particularly at high southern latitudes and in regions outside the principal observing routes. In each year, DINCAE recovers the dominant latitudinal temperature gradient, with warm tropical waters and cooler waters toward 60° latitude, as well as regional structures

https://doi.org/10.5194/essd-2026-617
Preprint. Discussion started: 25 November 2026
© Author(s) 2026. CC BY 4.0 License.



associated with major currents. The reconstructions provide spatially complete fields even during the sparsely observed early decades.

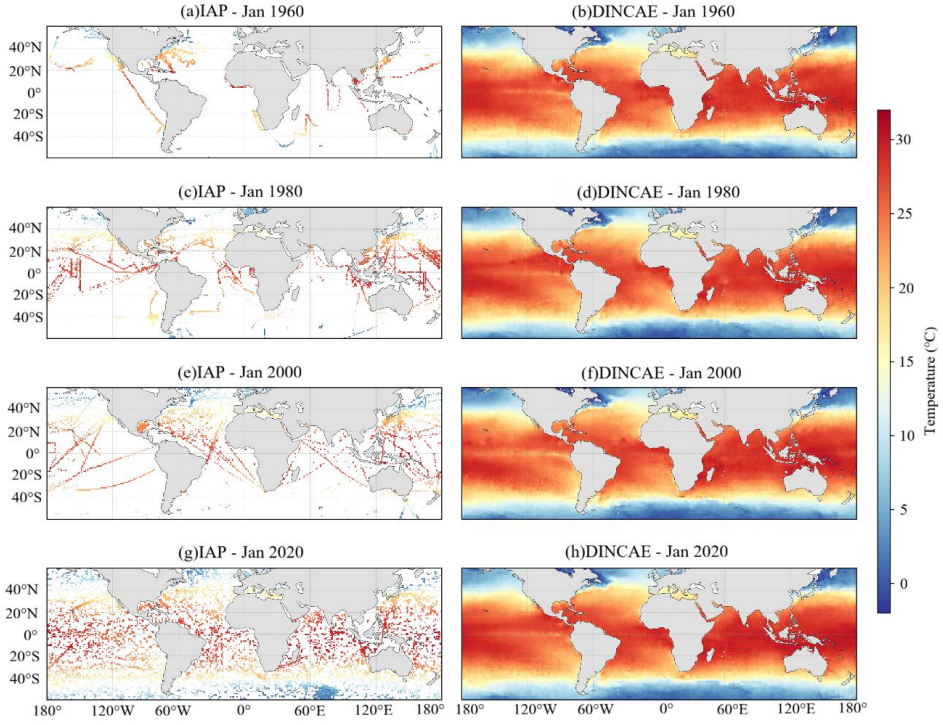

Figure 3: Comparison chart of reconstruction results

Model skill is assessed using the 15% withheld observations that are excluded from the reconstruction input. DINCAE is trained using the remaining 85% with the training configuration unchanged. Paired DINCAE estimates and withheld observations are used to calculate the RMSE,BIAS and CORR. Metrics are also summarized by decade to contrast the data-sparse pre-Argo period with the better-observed Argo period.Across all withheld values, DINCAE achieves an MAE of 0.58 °C, an RMSE of 0.87 °C, a correlation coefficient of 0.994, and R^2 of 0.989. Decadal comparisons with IAPv4.2 indicate that DINCAE has lower RMSE during much of the pre-Argo period, whereas IAPv4.2 performs better after the observing system becomes denser. DINCAE also shows a bias closer to zero in the early decades. Because withheld observations can only sample locations where measurements exist, these statistics may not represent performance in persistently unobserved regions.

https://doi.org/10.5194/essd-2026-617
Preprint. Discussion started: 25 November 2026
© Author(s) 2026. CC BY 4.0 License.



Open Access Earth System Science Data Discussions

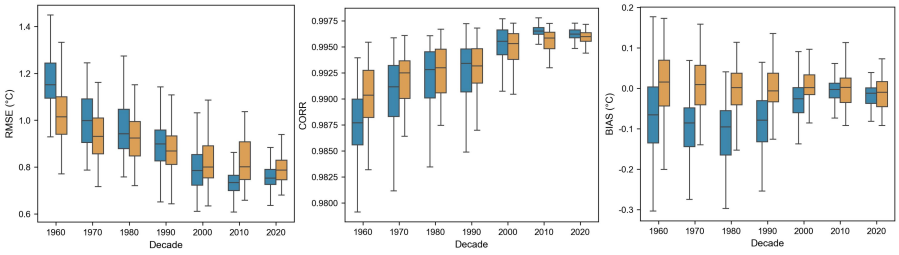

Figure 4: Comparison chart for evaluating the accuracy of reconstruction results

4.2 Climate logical annual cycle

The climatological annual cycles of 0–2000 m OHC during 2006–2020 are compared among OHC-DREC, IAPv4.2, Ishii, EN4.2, RG-Argo, GDCSM-Argo, NCEI, and BOA-Argo. The products show consistent seasonal phasing in the full analysis domain and in the two hemispheres. Northern Hemisphere OHC generally increases from boreal spring to early autumn, whereas Southern Hemisphere OHC follows the opposite phase. The partially compensating hemispheric cycles produce a smaller annual cycle in the 60° S–60° N total. OHC-DREC reaches a maximum in April and a minimum in August, with a peak-to-trough amplitude of 51.4 ZJ, compared with 59.5 ZJ for IAPv4.2. The corresponding amplitudes are 62.2 ZJ for Ishii, 55.8 ZJ for EN4.2, 69.2 ZJ for RG-Argo, 60.7 ZJ for GDCSM-Argo, and 63.4 ZJ for BOA-Argo. NCEI reaches its minimum in September and has an amplitude of 58.7 ZJ.

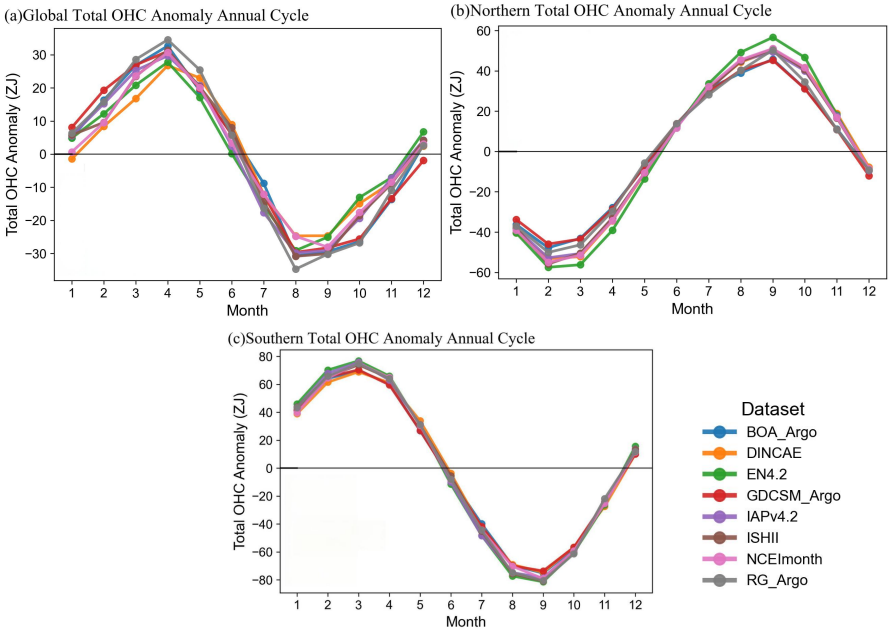

Figure 5: Climatological annual cycle of 0–2000 m OHC anomalies during 2006–2020 for (a) the 60° S–60° N analysis domain, (b) the Northern Hemisphere portion of the domain, and (c) the Southern Hemisphere

https://doi.org/10.5194/essd-2026-617
Preprint. Discussion started: 25 November 2026
© Author(s) 2026. CC BY 4.0 License.



portion. Values are in ZJ.

4.3 SST and ENSO diagnostics

Physically, SST is not a measurement at a single depth. Instead, it is divided is into multiple layers based on different heat conduction processes and observation methods. In this study, the temperature at a depth of 1-5 m below the sea surface was selected as the representative SST.

The reconstructed SSTA are compared with ERSSTv5, HadISST, COBE2, and the 1 m field from IAPv4.2 (Zhang et al., 2021). Because the reconstruction ends in October 2024, trends are calculated over the complete 1960–2023 period. The domain-mean trend of the reconstructed SST is 0.94 ± 0.10 °C century^{-1} (90% confidence interval), compared with 1.20 ± 0.10 °C century^{-1} for IAPv4.2 and 0.90–1.17 °C century^{-1} for the three independent SST products. All products show warming in the full domain and in the Pacific, Atlantic, Indian, and Southern Ocean sectors (Small et al., 2020) . The reconstructed SST trend is slightly weaker than that of IAPv4.2 but remains within the range of the independent products. Inter-product spread is largest in the Southern Ocean sector, consistent with sparse historical sampling there.

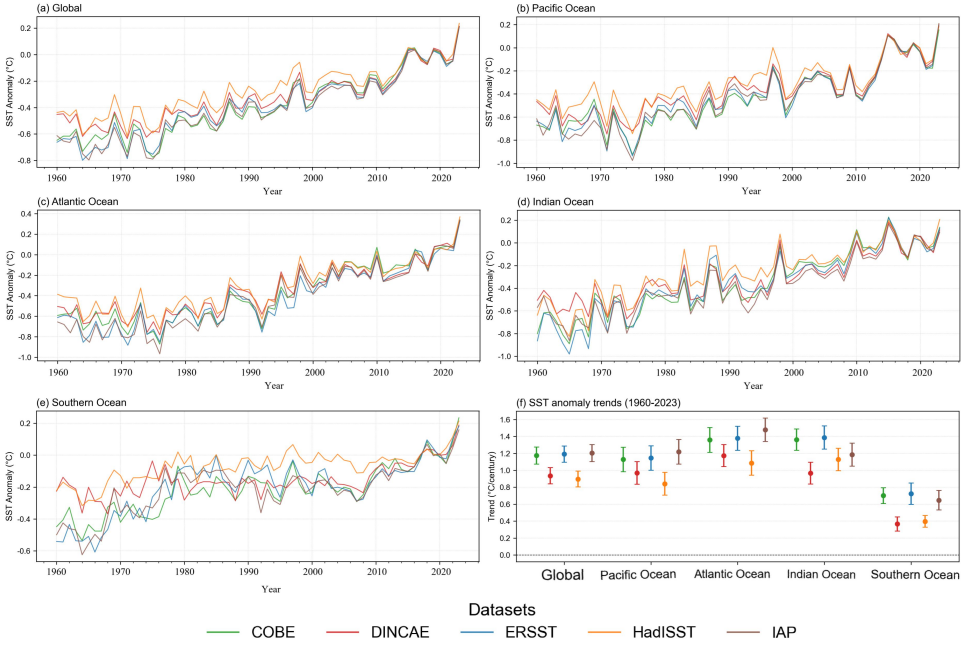

Figure 6: Annual SST anomalies from 1960 to 2023 for (a) the full 60° S–60° N domain, (b) the Pacific, (c) the Atlantic, (d) the Indian Ocean, and (e) the Southern Ocean sector, together with (f) linear trends and 90% confidence intervals.

The spatial trend patterns for 1960–2023 are broadly consistent among the reconstructed SST, ERSSTv5, HadISST, COBE2, and IAPv4.2. The products show pronounced warming in the North Sea,

https://doi.org/10.5194/essd-2026-617
Preprint. Discussion started: 25 November 2026
© Author(s) 2026. CC BY 4.0 License.

the Mediterranean Sea, the Gulf of Alaska, and several western boundary-current and coastal regions. The reconstructed SST shows weaker warming than some products in the Bohai and Yellow Seas and in the East Australian Current region, but its regional pattern is similar to ERSSTv5 and COBE2. HadISST and the reconstructed SST show more extensive cooling in parts of the Southern Ocean sector than the other products. Differences in these sparsely observed regions illustrate the sensitivity of long-term trends to sampling and reconstruction method.

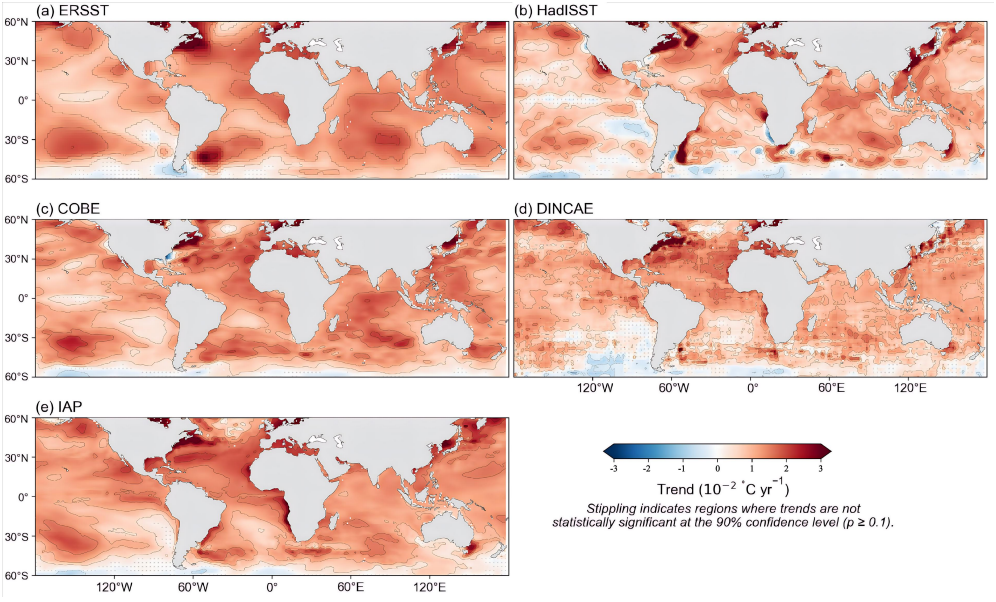

Figure 7: Linear trends in SST anomalies during 1960–2023 for (a) ERSSTv5, (b) HadISST, (c) COBE2, (d) the reconstructed SST, and (e) IAPv4.2. Trends are expressed in 10^{-2} °C yr^{-1}.

ENSO variability is evaluated using the Niño-3.4 index, defined as the mean SST anomaly over 5° N–5° S and 170° W–120° W. Indices calculated from the reconstructed SST and IAPv4.2 are compared with the NOAA ONI based on ERSSTv5. The correlation between the reconstructed SST and ONI is 0.8303, compared with 0.8298 between IAPv4.2 and ONI. The similar correlations indicate that both gridded products reproduce the principal ENSO variability, with a marginally higher correlation for the reconstructed SST.

The time series show larger differences during the sparsely observed 1960s and 1970s. IAPv4.2 is smoother during this period, whereas the reconstructed SST retains larger interannual fluctuations. This contrast is consistent with the different mapping frameworks: objective analysis can relax poorly constrained regions toward a climatological first guess, whereas the convolutional reconstruction uses spatial and temporal relationships learned from the available data. These early variations should nevertheless be interpreted cautiously because direct observational constraints are limited.

Several strong El Niño and La Niña events are examined to compare the amplitude of the reconstructed indices. During the 1982–1983 El Niño and the 1988–1989 La Niña, the reconstructed

https://doi.org/10.5194/essd-2026-617
Preprint. Discussion started: 25 November 2026
© Author(s) 2026. CC BY 4.0 License.



SST shows amplitudes closer to ONI than IAPv4.2. This result indicates less smoothing of strong events in the reconstructed SST, but it does not by itself establish that every reconstructed regional feature is more accurate in data-sparse periods.

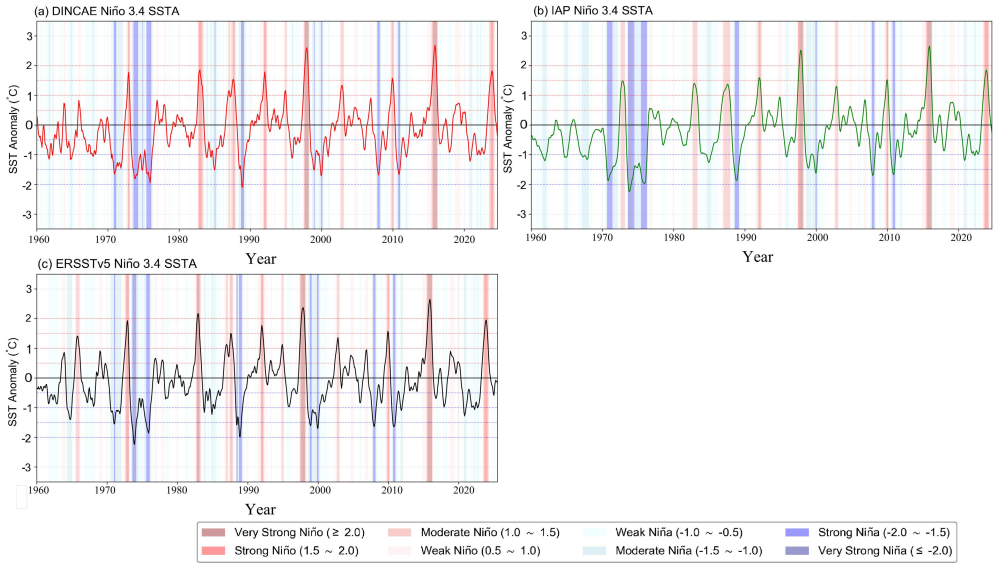

Figure 8: Analysis diagram of the correlation between SST products and ENSO

4.4 Global OHC time series

Figure 9 compares annual OHC anomalies in the 0–700 m and 0–2000 m layers from 1960 to 2023. All products show long-term warming, although the magnitude and interdecadal variability differ. Disagreement is largest before the widespread deployment of Argo, when historical temperature observations were sparse. OHC-DREC shows a smaller warming amplitude than most conventional products over the full 1960–2023 period.

For 1960–2023, the OHC-DREC warming trend is 3.03 ± 0.33 ZJ yr^{-1} in the 0–700 m layer, close to the EN4.2 estimate of 3.24 ± 0.35 ZJ yr^{-1}. IAPv4.2 and Ishii show larger trends of 4.10 ± 0.30 and 3.71 ± 0.23 ZJ yr^{-1}, respectively. In the 0–2000 m layer, OHC-DREC again gives the smallest trend, 4.05 ± 0.45 ZJ yr^{-1}, compared with 4.89 ± 0.539 ZJ yr^{-1} for EN4.2, 5.78 ± 0.41 ZJ yr^{-1} for IAPv4.2, and 5.88 ± 0.36 ZJ yr^{-1} for Ishii. These differences can arise from reconstruction methods, observational coverage, historical instrument-bias corrections, and reference-climatology choices.

During the Argo-dominated 2005–2023 period, the spread among products narrows. In the 0–700 m layer, the OHC-DREC trend is 6.16 ± 0.70 ZJ yr^{-1}, close to NCEI (6.31 ± 0.74), BOA-Argo (6.30 ± 0.74), GDCSM-Argo (6.13 ± 0.63), and RG-Argo (6.23 ± 0.73 ZJ yr^{-1}); Ishii, IAPv4.2, and EN4.2 give larger trends of 6.80 ± 0.59, 7.16 ± 0.64, and 7.44 ± 0.61 ZJ yr^{-1}, respectively. In the 0–2000 m layer, OHC-DREC (9.22 ± 0.66 ZJ yr^{-1}) is likewise close to NCEI (9.70 ± 0.83), BOA-Argo (9.65 ± 0.82),

https://doi.org/10.5194/essd-2026-617
Preprint. Discussion started: 25 November 2026
© Author(s) 2026. CC BY 4.0 License.



Open Access Earth System Science Data Discussions

GDCSM-Argo (9.68 ± 0.56), and RG-Argo (9.81 ± 0.93 ZJ yr^{-1}), whereas Ishii, IAPv4.2, and EN4.2 show trends of 10.83 ± 0.70, 10.68 ± 0.61, and 11.70 ± 0.62 ZJ yr^{-1}. The closer agreement after 2005 is consistent with the stronger observational constraint provided by Argo.

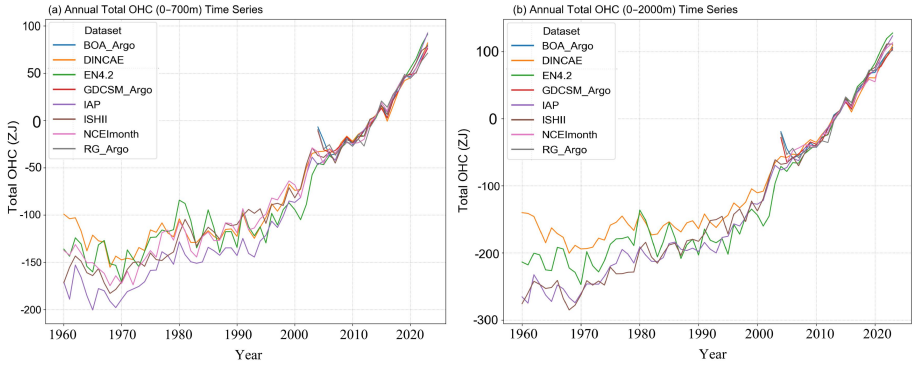

Figure 9: Annual OHC anomalies from 1960 to 2023 for (a) 0–700 m and (b) 0–2000 m.

During 1960–2023, OHC-DREC and IAPv4.2 show broadly consistent spatial trend patterns, with warming over approximately 90% of the analysed ocean area. The largest differences occur in the Southern Ocean sector, the North Indian Ocean, and energetic current systems. In the 0–2000 m layer, OHC-DREC generally shows weaker warming than IAPv4.2 in parts of the Southern Ocean sector. Patchy differences in the Kuroshio Extension and North Atlantic Current regions indicate sensitivity to mesoscale variability and to the reconstruction method. Both products show strong heat accumulation in the northwestern Atlantic and parts of the Southern Ocean sector, together with a cooling region in the subpolar North Atlantic commonly described as the North Atlantic warming hole(Jin et al., 2024).

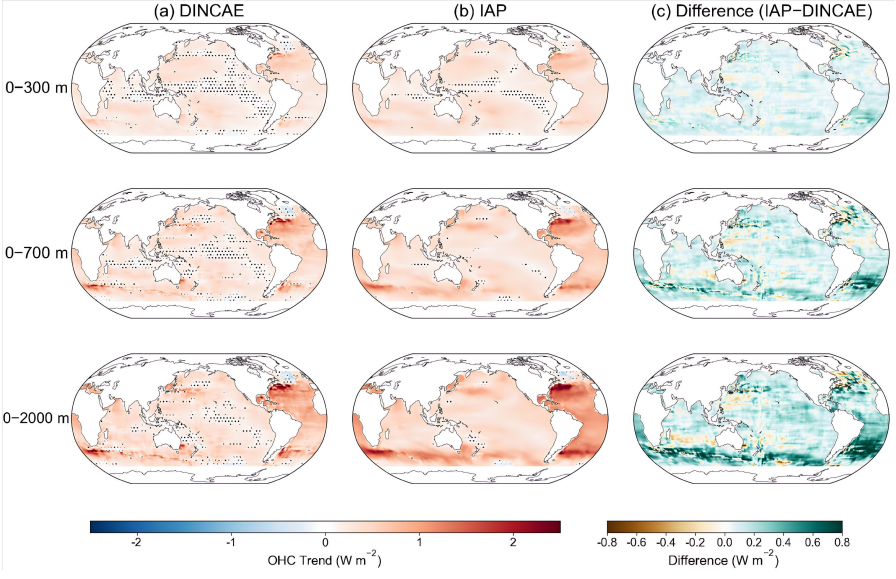

Figure 10: Linear OHC trends during 1960–2023 for the 0–300 m, 0–700 m, and 0–2000 m layers. Columns show (a) OHC-DREC, (b) IAPv4.2, and (c) IAPv4.2 minus OHC-DREC.

https://doi.org/10.5194/essd-2026-617
Preprint. Discussion started: 25 November 2026
© Author(s) 2026. CC BY 4.0 License.



During 1991–2023, OHC-DREC and IAPv4.2 retain similar large-scale trend patterns, with finer spatial structure than in the 1960–2023 comparison because observational coverage is denser. In the Pacific, the 0–300 m, 0–700 m, and 0–2000 m trends exhibit a west-warm/east-cool pattern associated with Pacific decadal variability: cooling extends across the central and eastern tropical Pacific and along parts of the eastern boundary, while warming dominates the western tropical and subtropical Pacific. This pattern may contain contributions from both internal variability and externally forced change, and the dataset comparison alone does not separate these mechanisms.

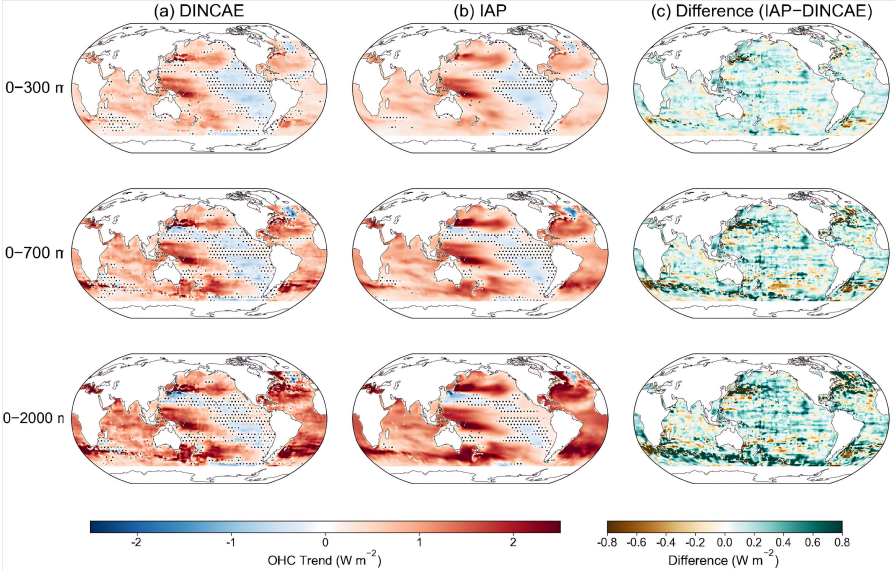

Figure 11: Linear OHC trends during 1991–2023 for the 0–300 m, 0–700 m, and 0–2000 m layers. Columns show (a) OHC-DREC, (b) IAPv4.2, and (c) IAPv4.2 minus OHC-DREC.

Interannual OHC variability in the tropical Pacific is strongly influenced by ENSO. Figure 12 shows latitude–time diagrams of 0–2000 m OHC anomalies averaged zonally across the tropical Pacific, together with ONI. In both OHC-DREC and IAPv4.2, positive OHC anomalies develop during major El Niño events and negative anomalies accompany La Niña events, indicating that the reconstructed heat-content variability is dynamically consistent with the ENSO cycle.

During the sparsely observed 1960s, OHC-DREC shows stronger and more spatially continuous ENSO-related signals than IAPv4.2. For the 1963–1964 and 1965–1966 El Niño events, positive anomalies in OHC-DREC evolve more coherently with ONI, whereas the IAPv4.2 signal is weaker and smoother. OHC-DREC also represents the eastward evolution of anomalies during the 1968–1969 event more clearly. These comparisons demonstrate that the convolutional reconstruction retains interannual structure under sparse sampling, while the model uncertainty remains important for evaluating individual early-period events.

https://doi.org/10.5194/essd-2026-617
Preprint. Discussion started: 25 November 2026
© Author(s) 2026. CC BY 4.0 License.



Open Access Earth System Science Data Discussions

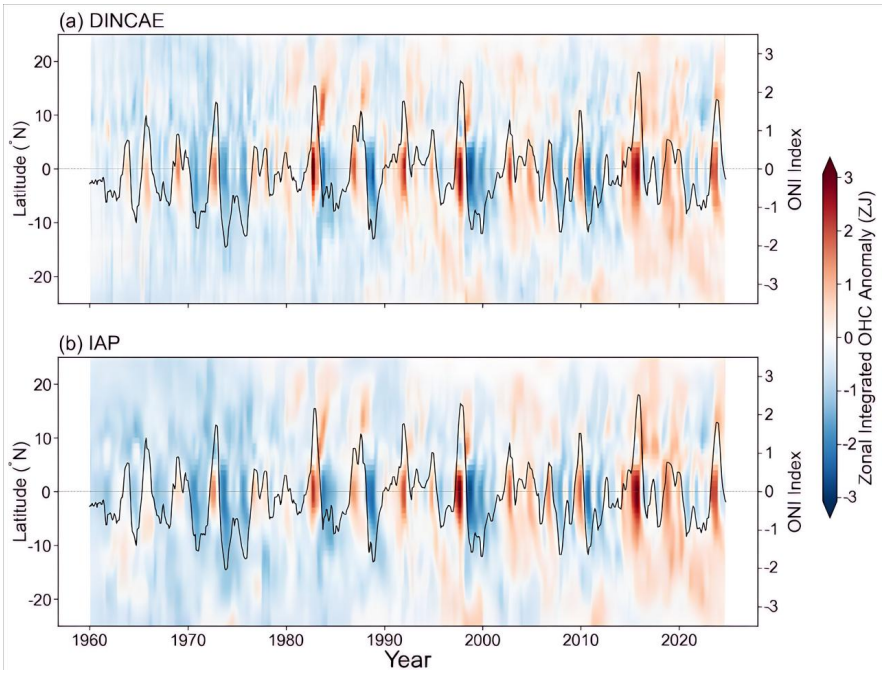

Figure 12: Hovmöller diagrams of zonally integrated 0–2000 m OHC anomalies in the tropical Pacific for (a) OHC-DREC and (b) IAPv4.2 during 1960–2024.

4.5 Ocean and Earth budget

The consistency between OHC change and Earth's energy imbalance is evaluated by comparing the OHC heating rate, dOHC/dt, with CERES EBAF. Monthly OHC is first converted to a centred 12-month mean referenced to June of each year, after which the forward difference between consecutive annual values is calculated. CERES data are averaged over the corresponding annual windows so that the two estimates have consistent temporal sampling.

The correlation reported in Fig. 13 is calculated after excluding 2016, which was treated as an anomalous high-leverage year in this comparison. With this stated exclusion, the correlation between the OHC-DREC heating rate and CERES Earth energy imbalance is 0.75, and is higher than the corresponding IAPv4.2–CERES correlation. OHC-DREC does not use sea-surface height, gravity, satellite altimetry, or CERES data as predictors; the agreement therefore provides an independent physical-consistency check on the profile-based reconstruction. Agreement is particularly close during 2005–2011, when the transition to the Argo observing system substantially increased the number and spatial coverage of temperature profiles.

https://doi.org/10.5194/essd-2026-617
Preprint. Discussion started: 25 November 2026
© Author(s) 2026. CC BY 4.0 License.



Open Access Earth System Science Data Discussions

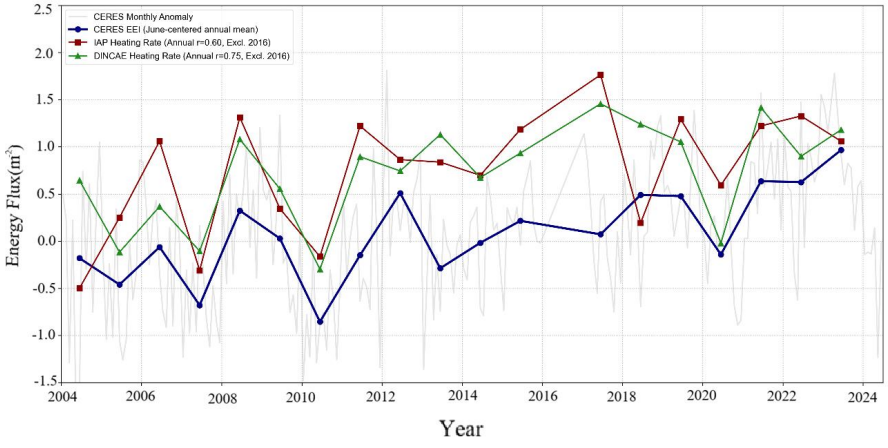

Figure 13: Comparison diagram of OHCT and CERES EEI data

5 Summary and discussion

This study reconstructs a three-dimensional monthly ocean temperature field from quality-controlled CODC-v2 profiles using DINCAE and evaluates derived the OHC from complementary perspectives. Skill is first measured against the 15% of valid temperature observations independently withheld and excluded from model fitting. Agreement of the annual cycle, long-term trend, and spatial pattern with independently produced OHC products then tests large-scale consistency, and the OHC rate of change is compared with the independent CERES Earth energy imbalance without other information as a model predictor.. Stronger performance after the Argo transition is physically expected because denser and more uniform profiles constrain the model more directly. In earlier sparse periods, convolutional filters can retain recurring regional structures learned across available times and locations, which helps explain why early ENSO-related variability can be less smoothed than a field relaxed toward a climatological first guess. These results support DINCAE as an alternative profile-based gridding framework, without implying that that it removes uncertainty in poorly constrained regions or depths.

Several limitations should be considered when using OHC-DREC. First, OHC is calculated using constant seawater density and specific heat capacity. This approximation is widely used for large-scale OHC analysis but neglects variations with temperature, salinity, and pressure and may introduce regional biases, particularly in the deep ocean and dynamically active regions. Second, uncertainty increases where historical profiles are sparse, especially at depth and near the southern boundary of the domain. The exported DINCAE temperature_error variable provides a model-derived grid-cell uncertainty, whereas withheld-observation residuals quantify performance only where observations are

https://doi.org/10.5194/essd-2026-617
Preprint. Discussion started: 25 November 2026
© Author(s) 2026. CC BY 4.0 License.



397 available; the two measures should not be interpreted as equivalent (Samuel & Karen, 2022) . Third,
398 the 1° × 1° grid cannot fully resolve mesoscale and smaller-scale variability in western boundary
399 currents and other energetic regions. Future versions could incorporate variable thermodynamic
400 properties, additional deep-ocean observations, and regionally refined reconstructions.

401 Overall, OHC-DREC provides a profile-based, spatially complete monthly reconstruction of
402 ocean temperature and OHC for 60° S–60° N from 1960 to 2024. Its principal value lies in combining a
403 common reconstruction framework with observation-based validation, model-derived uncertainty, and
404 comparisons against independent temperature, OHC, ENSO, and energy-budget products.

405 **Appendix A. Reproducibility information for DINCAE training**

406 DINCAE is a convolutional neural-network method that can be trained directly on incomplete
407 geophysical fields and produces both reconstructed values and error estimates (Barth et al., 2020).
408 DINCAE 2.0 introduces additive skip connections and refinement steps that improve the transfer of
409 fine-scale information through the encoder–decoder architecture (Barth et al., 2022).

410 In this study, the original DINCAE 2.0 gridded-data tutorial implementation is applied separately
411 at the 79 target depths to reconstruct monthly ocean temperature. Each depth is represented on a 120 ×
412 360 grid covering 60° S–60° N. The model uses a U-Net-like convolutional encoder–decoder with
413 additive skip connections and the tutorial's two-step refinement model.

414 The workflow comprises three stages: preparation of the monthly gridded input fields, model
415 training and validation, and reconstruction with uncertainty output.

416 (1) Monthly gridded-data preparation

417 The inputs include monthly gridded temperature, longitude, latitude, time, and a land–ocean mask.
418 At each depth, the data array contains 120 latitude cells, 360 longitude cells, and 778 monthly samples.
419 A three-sample time window supplies the previous, current, and following monthly fields. Table 3 lists
420 the 10 input channels used by DINCAE.

421

Number	variable
1	Sea temperature scaled by the reciprocal of the error variance
2	The reciprocal of the error variance
3	Sea temperature scaled by the reciprocal of the error variance on the previous day
4	The reciprocal of the error variance of the previous day
5	Sea temperature scaled by the reciprocal of the error variance on the next day
6	The reciprocal of the error variance of the next day
7	Longitude (linearly scaled between -1 and 1)
8	Latitude (linearly scaled between -1 and 1)

https://doi.org/10.5194/essd-2026-617
Preprint. Discussion started: 25 November 2026
© Author(s) 2026. CC BY 4.0 License.



Open Access Earth System Science Data Discussions

9	The cosine value of the nth day of the year divided by 365.25.
10	The sine value of the nth day of the year divided by 365.25.

Table 3. Specific input variable of DINCAE

(2) Model training stage

The training of the DINCAE model is an iterative optimization process. Thanks to the parallel computing architecture of GPUs, the training speed of this process has been greatly improved. However, due to the limited GPU memory, small batches of data are used for training. The network is optimized in parallel on the GPU, and Gaussian noise (jitter_std = 0.05) is added to simulate uncertainty. The cross-validation dataset is used to calculate the loss. The encoding layer and the decoding layer are introduced respectively according to the autoencoder structure.

The encoding layer is mainly used to gradually compress the spatial dimension of the input data while extracting key features. The encoder part of DINCAE includes multiple convolutional layers and pooling layers. Convolutional layers are used to extract features, and the spatial resolution is gradually reduced through pooling layers (downsampling). Convolutional layers are used to extract the spatial features of the data. The encoder contains 5 convolutional layers, and each convolutional layer contains a different number of filters and a fixed convolution kernel size of 3×3. The number of filters in each convolutional layer gradually increases, which are (32, 64, 128, 256, 512) respectively. The increase in the number of these filters is to extract more feature information at a lower spatial resolution. The convolution kernel slides on the input data and extracts local features. The pooling layer uses a 2×2 pooling window and a 2×2 stride. In this study, max-pooling is used. The pooling layer is mainly used for downsampling and compressing the data spatial dimension. The output size of each pooling layer is half of the output of the previous convolutional layer. For example, from 120×360 to 60×180, then to 30×90, and so on. The pooling layer can reduce the data dimension and the amount of calculation, improve the computational efficiency, and at the same time retain the main feature information.

The task of the decoder is to restore the data using the latent representation of the encoder and recover the spatial structure information. The decoder includes de-convolutional or interpolation layers and skip-connection layers. The interpolation layer plays a role of reverse expansion in the decoder, gradually restoring the spatial resolution of the data. For example, the interpolation layer expands the data of size 4×12 to 8×24, and then to a higher resolution. The interpolation layer uses the nearest-neighbor interpolation algorithm to increase the data size. This is opposite to the convolutional pooling layer and can gradually restore the compressed features. This study uses the optimized DINCAE 2.0 method. Compared with DINCAE 1.0, it changes to an additive skip-connection. The skip-connection directly adds the output of a specific layer in the encoder to the output of a certain layer in the decoder, retaining the detailed information at the original resolution, preventing the loss of small-scale details in the reconstruction, and reducing the vanishing gradient. The skip-connection can compensate for the detailed information lost in

https://doi.org/10.5194/essd-2026-617
Preprint. Discussion started: 25 November 2026
© Author(s) 2026. CC BY 4.0 License.



457 the encoding process during decoding, thereby improving the quality of data reconstruction. This
458 study adopts the additive skip-connection method. The additive skip-connection adds the output of
459 the encoder layer to the output of the decoder layer instead of simple splicing. This operation
460 simplifies the feature merging process, saves the computational cost, and avoids the problem of a
461 sharp increase in the channel dimension of the feature map.

$$\mathbf{X}^{(l+1)}=f^{(l)}\left(\mathbf{X}^{(l)}\right)+\mathbf{X}^{(l)}. \tag{1}$$

462 The convolutional layers in the decoder are used to further process the data obtained after
463 interpolation and skip connections, making it gradually approach the structure of the original input
464 data. All convolutional layers, including those in the decoding process, use the most common
465 activation function in convolutional layers, which is the standard Rectified Linear Unit (ReLU)
466 function.

467 (3) Missing data reconstruction stage

468 The output layer outputs two variables, which are the sea temperature anomaly value divided
469 by the error variance and the logarithm of the reciprocal of the expected error variance. The
470 formulas for calculating the reconstructed temperature value and the error variance of the
471 reconstructed data are as follows:

$$\hat{y}_{ij}=T_{ij1}^{(out)}\cdot\ \sigma_{ij}^{2} \tag{2}$$

$$\sigma_{ij}^{2}=\frac{1}{max\left(exp\left(min\left(T_{ij2}^{(out)},\gamma\right)\right),\delta\right)} \tag{3}$$

472 $\hat{y}_{ij}$ represents the reconstructed temperature value;σ_{ij}^{2} represents the error variance of the
473 reconstructed data; set the γ value to 10; set the δ to 10^{-3};$T_{ij1}^{(out)}$ represents the anomaly value of
474 sea temperature divided by the error variance;$T_{ij2}^{(out)}$ represents the logarithm of the reciprocal of
475 the variance of the representative expected error. The subscripts *i* and *j* represent the positions of
476 each grid, and max and min represent the maximum and minimum functions.

477 The model uses the backpropagation algorithm to iteratively optimize the results of the
478 output layer to continuously improve its reconstruction accuracy. Instead of using the standard L2
479 or L1 cost function, the network is trained by minimizing the negative log-likelihood of a
480 Gaussian distribution with a mean of $\hat{y}_{ij}$ and a variance of $\hat{\sigma}_{ij}$ During the optimization process,
481 DINCAE uses the cross-validation dataset to calculate the loss for model optimization. The
482 formula for the loss function is as follows:

https://doi.org/10.5194/essd-2026-617
Preprint. Discussion started: 25 November 2026
© Author(s) 2026. CC BY 4.0 License.



$$J(\hat{y}_{ij},\hat{\sigma}_{ij})=\&\frac{1}{2N}\sum_{ij}[(\frac{y_{ij}-\hat{y}_{ij}}{\hat{\sigma}_{ij}})^2+\log f_0(\hat{\sigma}_{ij}^2)+2\log f_0(\sqrt{2\pi})]. \quad (4)$$

The first term in the loss function measures the error between the observed values and the reconstructed values, which is similar to the Mean Squared Error (MSE). However, here each error is normalized by its estimated standard deviation. The second term controls the magnitude of the error estimate to prevent the network from producing overly large error variances. The third term is a constant term that maintains mathematical integrity but has no impact on the optimization process.

Use the initially reconstructed $\hat{y}_{ij}$ and $\hat{\sigma}_{ij}^2$ as new inputs, and pass them to the second autoencoder along with the original input data. This is equivalent to increasing the number of input data parameters from the original 10 to 12. The second autoencoder generates new reconstruction results $\hat{y}_{ij}^{'}$and$\widehat{\sigma}_{ij}^{'2}$. The loss function combines the results of the two stages to ensure that each reconstruction can optimize the output of the model. The multi-level loss function for the refinement step is as follows:

$$J_r=\alpha J(\hat{y}_{ij},\hat{\sigma}_{ij}^2)+\alpha^{'}J\left(\hat{y}_{ij}^{'},\widehat{\sigma}_{ij}^{'2}\right) \quad (5)$$

Training uses the Adam optimizer. No explicit L1 or L2 weight regularisation is applied; the Gaussian jitter added to the input fields (jitter_std = 0.05) serves as a stochastic regulariser during training.

Data availability

The OHC-DREC dataset generated in this study is available from the Zenodo open-access repository under the concept DOI: https://doi.org/10.5281/zenodo.21758104 (Xie et al., 2026). This DOI represents all versions of the dataset and will always resolve to the latest version. For the peer-review process, the dataset can be accessed via the following anonymous review link: https://zenodo.org/records/21758104?token=eyJhbGciOiJIUzUxMiJ9.eyJpZCI6ImQyYzliOGM2LTc4M2ItNDgwYi1iOGUyLTY3MzI2MTg2YTU5MCIsImRhdGEiOnt9LCJyYW5kb20iOiIzOTQ4NDZhYzI3YmRiM2QzYzU0YTIzZDM5YzgxOGYyMyJ9.ngWXGXLM9loMWxHEqk6YuRCSvUK92AuESL3SXSubEEGaoRndxVwGFvSZJTvTg3OERP1U6IrI0A9Hy6ELh3R4Mg. The data are released under a CC BY 4.0 license.

https://doi.org/10.5194/essd-2026-617
Preprint. Discussion started: 25 November 2026
© Author(s) 2026. CC BY 4.0 License.



Author Contribution

Conceptualization, T.X. and H.Y.; methodology, T.X. and W.M.; software, W.M. and J.L.; validation, W.M., W.L., and Y.C.; formal analysis, Y.H. and X.Z.; investigation, M.H. and H.L.; data curation, W.M. and J.L.; writing—original draft preparation, T.X.; writing—review and editing, H.Y., M.H., and T.X.; visualization, W.M. and Y.C.; supervision, H.Y.; project administration, T.X.; funding acquisition, T.X.

Competing interests

The authors declare that they have no conflict of interest.

Financial support

This research was financially supported by the Natural Science Research Start-up Foundation of Recruiting Talents of Nanjing University of Posts and Telecommunications (grant no. NY226003) and the Open Fund Project of Key Laboratory of Marine Environmental Information Technology, Ministry of Natural Resources of the People's Republic of China.

References

Abraham, J. P., et al. (2013). A review of global ocean temperature observations: Implications for ocean heat content estimates and climate change. Reviews of Geophysics, 51, 450–483. https://doi.org/10.1002/rog.20022

Allan, R. P., & Merchant, C. J. (2025). Reconciling Earth's growing energy imbalance with ocean warming. Environmental Research Letters, 20, 044002. https://doi.org/10.1088/1748-9326/adb448

Allison, L. C., Roberts, C. D., Palmer, M. D., Hermanson, L., Killick, R., Rayner, N. A., Smith, D. M., & Andrews, M. B. (2019). Towards quantifying uncertainty in ocean heat content changes using synthetic profiles. Environmental Research Letters, 14(8). https://doi.org/10.1088/1748-9326/ab2b0b

Barth, A., Alvera-Azcárate, A., Licer, M., et al. (2020). DINCAE 1.0: a Convolutional Neural Network with Error Estimates to Reconstruct Sea Surface Temperature Satellite observations. Geoscientific Model Development, 13(3), 1609–1622. https://doi.org/10.5194/gmd-13-1609-2020

Barth, A., Alvera-Azcárate, A., Troupin, C., et al. (2022). DINCAE 2.0: Multivariate Convolutional Neural Network with Error Estimates to Reconstruct Sea Surface Temperature Satellite and Altimetry Observations. Geoscientific Model Development, 15(5), 2183–2196. https://doi.org/10.5194/gmd-15-2183-2022

Boyer, T., et al. (2016). Sensitivity of Global Upper-Ocean Heat Content Estimates to Mapping

https://doi.org/10.5194/essd-2026-617
Preprint. Discussion started: 25 November 2026
© Author(s) 2026. CC BY 4.0 License.



539 Methods, XBT Bias Corrections, and Baseline Climatologies. Journal of Climate, 29, 4817–4842.
540 https://doi.org/10.1175/JCLI-D-15-0801.1
541 Cheng, L., & Zhu, J. (2016). Benefits of CMIP5 Multimodel Ensemble in Reconstructing Historical
542 Ocean Subsurface Temperature Variations. Journal of Climate, 29(15), 5393–5416.
543 https://doi.org/10.1175/JCLI-D-15-0730.1
544 Cheng, L., et al. (2017). Improved estimates of ocean heat content from 1960 to 2015. Science
545 Advances, 3(3), e1601545. https://doi.org/10.1126/sciadv.1601545
546 Cheng, L., Abraham, J., Hausfather, Z., & Trenberth, K. E. (2019). How fast are the oceans warming?
547 Science, 363(6423), 128–129. https://doi.org/10.1126/science.aav7619
548 Cheng, L., Pan, Y., Tan, Z., et al. (2024). IAPv4 Ocean Temperature and Ocean Heat Content Gridded
549 Dataset. Earth System Science Data Discussions, 2024, 1–56. https://doi.org/10.5194/essd-16-3517-
550 2024
551 Colfescu, I., Christensen, H., & Gagne, D. J. (2024). A Machine Learning-Based Approach to Quantify
552 ENSO Sources of Predictability. Geophysical Research Letters, 51(13).
553 https://doi.org/10.1029/2023GL105194
554 Dergiades, T., Kaufmann, R. K., & Panagiotidis, T. (2016). Long-run changes in radiative forcing and
555 surface temperature: The effect of human activity over the last five centuries. Journal of Environmental
556 Economics and Management, 76, 67–85. https://doi.org/10.1016/j.jeem.2015.11.005
557 Domingues, C. M., Church, J. A., White, N. J., et al. (2008). Improved Estimates of Upper-ocean
558 Warming and Multi-Decadal Sea-Level Rise. Nature, 453(7198), 1090–1093.
559 https://doi.org/10.1038/nature07080
560 Forney, K. R., Miller, W. P., & Smith, A. T. (2025). The Increase in Global Ocean Heat Content and
561 Favorable Conditions for Tropical Cyclone and CYCLOP Intensification: Accounting for El Niño.
562 Journal of Marine Science and Engineering, 13(10), 1918. https://doi.org/10.3390/jmse13101918
563 Good, S. A., Martin, M. J., & Rayner, N. A. (2013). EN4: Quality Controlled Ocean Temperature and
564 Salinity Profiles and monthly Objective Analyses with Uncertainty Estimates. Journal of Geophysical
565 Research: Oceans, 118(12), 6704–6716. https://doi.org/10.1002/2013JC009067
566 Gouretski, V., & Reseghetti, F. (2010). On depth and temperature biases in bathythermograph data:
567 Development of a new correction scheme based on analysis of a global ocean database. Deep Sea
568 Research Part I: Oceanographic Research Papers, 57(6), 812–833.

https://doi.org/10.5194/essd-2026-617
Preprint. Discussion started: 25 November 2026
© Author(s) 2026. CC BY 4.0 License.



https://doi.org/10.1016/j.dsr.2010.03.011

Ishii, M., Shouji, A., Sugimoto, S., et al. (2005). Objective Analyses of Sea-Surface Temperature and Marine Meteorological Variables for the 20th century using ICOADS and the Kobe Collection. International Journal of Climatology, 25(7), 865–879. https://doi.org/10.1002/joc.1169

Ishii, M., & Kimoto, M. (2009). Reevaluation of historical ocean heat content variations with time-varying XBT and MBT depth bias. Journal of Oceanography, 65, 287–299. https://doi.org/10.1007/s10872-009-0027-7

Jin, F. (1997). An Equatorial Ocean Recharge Paradigm for ENSO. Part I: Conceptual Model. Journal of the Atmospheric Sciences, 54, 811–829. https://doi.org/10.1175/1520-0469(1997)054<0811:aeorpf>2.0.co;2

Jin, Y., Li, Y., Cheng, L., et al. (2024). Ocean Heat Content Increase of the Maritime Continent Since the 1990s. Geophysical Research Letters, 51(6). https://doi.org/10.1029/2023GL107526

Kato, S., Rose, F. G., Rutan, D. A., et al. (2018). Surface Irradiances of Edition 4.0 Clouds and the Earth's Radiant Energy System (CERES) Energy Balanced and Filled (EBAF) Data Product. Journal of Climate, 31(11), 4501–4527. https://doi.org/10.1175/JCLI-D-17-0208.1

Levitus, S., Antonov, J. I., Boyer, T. P., et al. (2012). World Ocean Heat Content and Thermosteric Sea Level Change (0–2000 m), 1955–2010. Geophysical Research Letters, 39(10), L10603. https://doi.org/10.1029/2012GL051106

Li, H., Xu, F., Zhou, W., et al. (2017). Development of a Global Gridded Argo Data Set with Barnes Successive Corrections. Journal of Geophysical Research: Oceans, 122(2), 866–889. https://doi.org/10.1002/2016JC012285

Li, Y., Church, J. A., McDougall, T. J., & Barker, P. M. (2022). Sensitivity of observationally based estimates of ocean heat content and thermal expansion to vertical interpolation schemes. Geophysical Research Letters, 49, e2022GL101079. https://doi.org/10.1029/2022GL101079

Liu, W. (2003). The Effect of Selective Cutting on the Carbon Budget of a Northern Hardwood Forest. Senior Thesis, Environmental Science and Public Policy, Harvard University. https://atmos.seas.harvard.edu/publications/effect-selective-cutting-carbon-budget-northern-hardwood-forest

Liu, W., Xie, S.-P., & Lu, J. (2016). Tracking ocean heat uptake during the surface warming hiatus. Nature Communications, 7, 10926. https://doi.org/10.1038/ncomms10926

https://doi.org/10.5194/essd-2026-617
Preprint. Discussion started: 25 November 2026
© Author(s) 2026. CC BY 4.0 License.



599 Loeb, N. G., Thorsen, T. J., Norris, J. R., Wang, H., & Su, W. (2018). Changes in Earth's Energy
600 Budget during and after the "Pause" in Global Warming: An Observational Perspective. Climate, 6, 62.
601 https://doi.org/10.3390/cli6030062
602 Lu, W., & Su, H. (2023). Ocean Heat Content Retrieval from Remote Sensing Data Based on Machine
603 Learning. In Artificial Intelligence Oceanography, 125–145. https://doi.org/10.1007/978-981-19-6375-
604 9_6
605 Lyman, J. M., & Johnson, G. C. (2023). Global High-Resolution Random Forest Regression Maps of
606 Ocean Heat Content Anomalies Using In Situ and Satellite Data. Journal of Atmospheric and Oceanic
607 Technology, 40, 575–586. https://doi.org/10.1175/JTECH-D-22-0058.1
608 Meehl, G. A., Arblaster, J. M., Fasullo, J. T., Hu, A., & Trenberth, K. E. (2011). Model-based evidence
609 of deep-ocean heat uptake during surface-temperature hiatus periods. Nature Climate Change, 1, 360–
610 364. https://doi.org/10.1038/nclimate1229
611 Merchel M, Walczowski W and Wieczorek P (2025) Anchored Argo profiling float experiments in the
612 southern Baltic Sea: Puck Bay and Hel Peninsula. Front. Mar. Sci. 12:1569261. doi:
613 10.3389/fmars.2025.1569261
614 Palmer, M. D., Haines, K., Tett, S. F. B., et al. (2007). Isolating the Signal of Ocean Global Warming.
615 Geophysical Research Letters, 34(23), L23610. https://doi.org/10.1029/2007GL031712
616 Palmer, M. D., McNeall, D. J., & Dunstone, N. J. (2011). Importance of the deep ocean for estimating
617 decadal changes in Earth's radiation balance. Geophysical Research Letters, 38, L13707.
618 https://doi.org/10.1029/2011GL047835
619 Rhein, M., Rintoul, S. R., Aoki, S., et al. (2013). Observations: Ocean. In Stocker, T. F., Qin, D.,
620 Alexander, Lisa & Allen, Simon & Bindoff, Nathaniel & Breon, Francois-Marie & Church, John &
621 Cubasch, Ulrich & Emori, Seita & Forster, Piers & Friedlingstein, Pierre & Gillett, Nathan & Gregory,
622 Jonathan & Hartmann, Dennis & Jansen, Eystein & Kirtman, Ben & Knutti, Reto & Kanikicharla,
623 Krishna & Lemke, Peter & Marotzke, Jochem & Masson-Delmotte, Valerie & Xie, Shang-Ping. (2013).
624 Climate change 2013: The physical science basis, in contribution of Working Group I (WGI) to the
625 Fifth Assessment Report (AR5) of the Intergovernmental Panel on Climate Change (IPCC).
626 Roemmich, D., & Gilson, J. (2009). The 2004–2008 Mean and Annual Cycle of Temperature, Salinity,
627 and Steric Height in the Global Ocean from the Argo Program. Progress in Oceanography, 82(2), 81–
628 100. https://doi.org/10.1016/j.pocean.2009.03.004

https://doi.org/10.5194/essd-2026-617
Preprint. Discussion started: 25 November 2026
© Author(s) 2026. CC BY 4.0 License.



629 Samuel, B., & Karen, M. (2022). Hierarchical Bayesian Modeling of Ocean Heat Content and its
630 Uncertainty. The Annals of Applied Statistics, 16(4), 2603–2625. https://doi.org/10.1214/22-
631 AOAS1605
632 Small, R. J., Bryan, F. O., Bishop, S. P., Larson, S., & Tomas, R. A. (2020). What Drives Upper-Ocean
633 Temperature Variability in Coupled Climate Models and Observations? Journal of Climate, 33(2), 577–
634 596. https://doi.org/10.1175/JCLI-D-19-0295.1
635 Su, H., Qin, T., Wang, A., & Lu, W. (2021). Reconstructing Ocean Heat Content for Revisiting Global
636 Ocean Warming from Remote Sensing Perspectives. Remote Sensing, 13(19), 3799.
637 https://doi.org/10.3390/rs13193799
638 Tan, Z. T., Cheng, L., Viktor, G., et al. (2023). A new Automatic Quality Control System for Ocean
639 Profile Observations and Impact on Ocean Warming Estimate. Deep-Sea Research Part I, 194.
640 https://doi.org/10.1016/j.dsr.2022.103961
641 Tan, Z., Zhu, Y., Cheng, L., et al. (2025). CODC-S: A Quality-Controlled Global Ocean Salinity
642 Profiles Dataset. Scientific Data, 12(1), 917. https://doi.org/10.1038/s41597-025-05172-9
643 Trenberth, K. E., & Fasullo, J. T. (2013). An apparent hiatus in global warming? Earth's Future, 1, 19–
644 32. https://doi.org/10.1002/2013EF000165
645 von Schuckmann, K., Palmer, M. D., Trenberth, K. E., et al. (2016). An imperative to monitor Earth's
646 energy imbalance. Nature Climate Change, 6, 138–144. https://doi.org/10.1038/nclimate2876
647 Wang, G., Cheng, L., et al. (2018). Consensus and Discrepancies of Basin-Scale Ocean Heat Content
648 Changes in Different Ocean Analyses. Climate Dynamics, 50(7–8), 2471–2487.
649 https://doi.org/10.1007/s00382-017-3751-5
650 Xie, S. (1994). Oceanic Response to the Wind Forcing Associated with the Intertropical Convergence
651 Zone in the Northern Hemisphere. Journal of Geophysical Research: Oceans, 99(C10), 20393–20402.
652 https://doi.org/10.1029/94JC01653
653 Xie, T., Mao, W., Yan, H., Hong, M., Li, J., Li, W., Chen, Y., Huang, Y., Zhu, X., & Li, H. (2026).
654 OHC-DREC: A three-dimensional ocean temperature reconstruction and ocean heat content dataset
655 from 1960 to 2024 [Data set]. Zenodo. https://doi.org/10.5281/zenodo.21758103
656 Zhang, B., Cheng, L., Tan, Z., et al. (2024). CODC-v1: a Quality-Controlled and Bias-Corrected Ocean
657 Temperature Profile Database from 1940–2023. Scientific Data, 11(1), 666.
658 https://doi.org/10.1038/s41597-024-03494-8

https://doi.org/10.5194/essd-2026-617
Preprint. Discussion started: 25 November 2026
© Author(s) 2026. CC BY 4.0 License.



659 Zhang, C., Wang, D., Liu, Z., et al. (2022). Global Gridded Argo Dataset Based on Gradient-Dependent
660 Optimal Interpolation. Journal of Marine Science and Engineering, 10(5), 650.
661 https://doi.org/10.3390/jmse10050650
662 Zhu, C., et al. (2024). Enhanced ocean heat storage efficiency during the last deglaciation. Science
663 Advances, 10, eadp5156. https://doi.org/10.1126/sciadv.adp5156